Transition from Boundary-Driven to Bulk-Driven Acoustic Streaming Due to Nonlinear Thermoviscous Effects at High Acoustic Energy Densities

Jonas Helboe Joergensen[1,*] Wei Qiu[2,†] and Henrik Bruus[1,‡]

[1]*Department of Physics, Technical University of Denmark, DTU Physics Building 309, DK-2800 Kongens Lyngby, Denmark*
[2]*Department of Biomedical Engineering, Lund University, Ole Römers väg 3, 22363, Lund, Sweden*

Acoustic streaming at high acoustic energy densities E_{ac} is studied in a microfluidic channel. It is demonstrated theoretically, numerically, and experimentally with good agreement that frictional heating can alter the streaming pattern qualitatively at high E_{ac} above 400 J/m³. The study shows how as a function of increasing E_{ac} at fixed frequency, the traditional boundary-driven four streaming rolls created at a half-wave standing-wave resonance transition into two large streaming rolls. This nonlinear transition occurs because friction heats up the fluid resulting in a temperature gradient, which spawns an acoustic body force in the bulk that drives thermoacoustic streaming.

Microscale acoustofluidic devices are used to manipulate and control microparticles and cells. In such devices, two main forces act on the suspended particles, the acoustic radiation force and the drag force due to acoustic streaming, which is a time-averaged flow caused by the inherent nonlinearities of fluid dynamics. Recent work has clarified many subtle details pertaining to the radiation force on microparticles, including thermoviscous effects [1] and microstreaming [2]. Concurrently, similar progress has been made in the theory of acoustic streaming, especially regarding thermoviscous effects. The fundamental boundary-driven streaming caused by time-averaged forces in the oscillatory boundary-layer flow [3], and the fundamental bulk-driven streaming generated by the time-averaged dissipation of traveling waves [4], have recently been supplemented by bulk-driven baroclinic [5,6] and thermoacoustic [7,8] streaming, caused by an interplay between standing acoustic waves and steady temperature gradients. However, as noted in Refs. [7,8], the validity of the conventional perturbation approach breaks down at moderately high, but experimentally obtainable average acoustic energy densities E_{ac} (1700 J/m³ is reported in Ref. [9]), or even lower, when combined with moderate thermal gradients above 1 K/mm. This need for an extension of the theory beyond perturbation theory is addressed in this Letter and in the jointly submitted paper [10] containing a detailed derivation of the nonperturbative model.

We introduce a nonperturbative iteration approach to investigate theoretically and numerically, the nonlinear effects appearing in a conventional acoustofluidic channel at high E_{ac} in the fluid, and we validate experimentally the model predictions. For general discussions, we consider a straight microchannel with arbitrary cross section embedded in an elastic solid driven at the standing half-wave acoustic resonance by actuating part of the exterior

surface. The streaming at low E_{ac} is dominated by conventional boundary-driven streaming with four streaming rolls as sketched in Figs. 1(a)–1(b). For specific numerical and experimental studies, we employ the widely used rectangular channel shown in Fig. 1(d) [10–14]. We show how nonlinear effects in the form of heating by viscous dissipation from the acoustic field inside the boundary layers set up a steady temperature gradient $\boldsymbol{\nabla} T_0$. This gradient drives a strong thermoacoustic streaming in the bulk, which changes the streaming flow qualitatively from

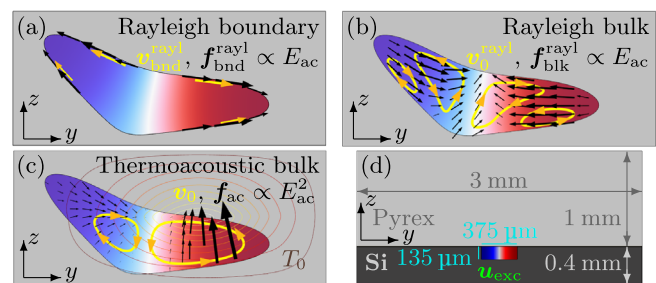FIG. 1. Cross section (yz) plots of the half-wave pressure resonance p_1 (blue-red), forces $\boldsymbol{f}$ (black arrows), and streaming $\boldsymbol{v}_0$ (yellow arrows and loops) inside a straight microchannel placed along x with an arbitrary yz cross-sectional shape in an elastic solid (gray). (a) Perturbative Rayleigh streaming ($\propto E_{ac}$): The boundary-layer force $\boldsymbol{f}_{bnd}^{rayl}$ and the streaming slip velocity $\boldsymbol{v}_{bnd}^{Rayl}$. (b) The response ($\propto E_{ac}$) in the bulk to $\boldsymbol{f}_{bnd}^{rayl}$: the viscous body force $\boldsymbol{f}_{blk}^{rayl}$ and four streaming rolls $\boldsymbol{v}_0^{rayl}$. (c) The nonperturbative thermoacoustic streaming $\boldsymbol{v}_0 \propto E_{ac}^2$ (two rolls) resulting from $\boldsymbol{f}_{ac}$ of Eq. (4a) driven by $\boldsymbol{\nabla} T_0$ of the temperature T_0 (contour lines). (d) The specific case of a rectangular water-filled channel embedded in a silicon-glass chip actuated by $\boldsymbol{u}_{exc}$ (green) at the bottom.

four to two flow rolls, as sketched in Fig. 1(c), and which by thermal convection alters the temperature field.

Our nonperturbative analysis of this nonlinear phenomenon and its underlying mechanism fills a knowledge gap in nonlinear acoustics, and it provides a guidance for understanding and optimizing acoustofluidic systems running at high E_{ac} such as high-intensity ultrasound focusing [15–17], acoustic streaming-based micromixers [18–21], particle manipulation devices [22–24], and high-throughput acoustophoresis devices [25–27].

Physical model.—The fluid in the microchannel in Fig. 1 is characterized by nine material parameters: density ρ, thermal conductivity k_{th}, specific heat c_p, dynamic and bulk viscosity η and η^b, thermal expansion coefficient α_p, the ratio of specific heats $\gamma = c_p/c_v$, and the isentropic and isothermal compressibility κ_s and $\kappa_T = \gamma\kappa_s$. The elastic solid is characterized by density ρ, longitudinal and transverse sound speed c_{lo} and c_{tr}, thermal conductivity kth, thermal expansion coefficient α_{p0}, and isothermal compressibility κ_T. For specific experimental and numerical studies, we consider the 24-mm long, silicon-glass chip used in Ref. [28] with the rectangular cross section; see Fig. 1(d). The horizontal half-wave resonance mode in the fluid (water) is excited at frequency $f_0 = 1.911$ MHz by a nanometric bottom-edge actuation displacement $\boldsymbol{u}_{exc}$. The response to the acoustic actuation is governed by the conservation equation for mass, momentum, and energy in the fluid and solid. The independent fields are the pressure p, the velocity $\boldsymbol{v}$, and the temperature T in the fluid, and the displacement $\boldsymbol{u}$ and T in the solid. The material parameters including temperature dependencies are given in Refs. [10,13] and in Table S1 in the Supplemental Material [29].

The iterative approach.—We exploit that the acoustic fields vary much faster ($\sim10^{-7}$ s) than the hydrodynamic and thermal flows ($\sim10^{-2}$ s). We study the steady limit of the slow timescale and decompose physical fields and material parameters Q_{phys} into a steady term Q_0 and a time-harmonic acoustic term $\mathrm{Re}\{Q_1 e^{-i\omega t}\}$ with a steady complex-valued amplitude Q_1,

$$Q_{phys}(t) = Q_0 + \mathrm{Re}\{Q_1 e^{-i\omega t}\}. \tag{1}$$

We neglect higher harmonics with angular frequency $n\omega$, $n = 2, 3, \ldots$, and use this ansatz to separate the governing equations in one set that controls the acoustic fields, and another set that controls the steady fields. Since products of two acoustic terms a_1 and b_1 contain a steady time-averaged part $\langle a_1 b_1 \rangle = \frac{1}{2}\mathrm{Re}\{a_1 b_1^*\}$, where the asterisk denotes complex conjugation, the acoustic terms appears as source terms $\langle a_1 b_1 \rangle$ in the governing equation of the steady fields. Conversely, the steady fields p_0, $\boldsymbol{v}_0$, and T_0 determine the material parameters on which the acoustic fields depend. In the nonperturbative thermoviscous model presented here, and with more details added in Sec. II-D in

Ref. [10], the combined set of equations for the coupled acoustic and steady fields are solved by a self-consistent iterative sequence until convergence is obtained. This procedure allows for studies beyond the traditional perturbative models of acoustofluidics [7,13].

Acoustofluidic systems also exhibit dynamics on two different length scales, one set by the system size and wavelength of the acoustic fields, $d \gtrsim 100$ μm, and another set by the viscous and thermal boundary layers of width $\delta_s = \sqrt{2\nu_0/\omega}$ and $\delta_t \approx \sqrt{2D^{th}/\omega}$, respectively ($\delta_t \lesssim \delta_s \lesssim 500$ nm $\ll d$). In the refined version of the iterative thermoviscous model presented in Ref. [10], we use this length-scale separation to decompose all fields Q into bulk and boundary-layer fields which varies on the scales d and δ, respectively, $Q = Q^d + Q^\delta$. The boundary-layer fields are solved analytically and then taken into account as effective boundary conditions on the bulk fields Q^d. This so-called *effective* boundary-layer model avoids the computationally costly resolution of the thin boundary layer, and is in practice a necessity to enable simulations in three dimensions (3D). Since in this Letter, we only perform simulations in two dimensions (2D), we do not decompose Q spatially, but instead use a so-called *full* model, in which the governing equations are solved numerically by resolving the boundary layers.

Acoustic and stationary fields.—The thermoviscous model is derived in detail in Ref. [10], but is briefly summarized here. The fluid stress is written $\boldsymbol{\sigma} = -\boldsymbol{\nabla} p + \boldsymbol{\tau}$, with $\boldsymbol{\tau} = \eta_0[\boldsymbol{\nabla}\boldsymbol{v} + (\boldsymbol{\nabla}\boldsymbol{v})^\mathsf{T}] + [\eta_0^b - \frac{2}{3}\eta_0](\boldsymbol{\nabla}\cdot\boldsymbol{v})\boldsymbol{I}$ being the viscous part. Inserting $\boldsymbol{v} = \boldsymbol{v}_0 + \boldsymbol{v}_1$ and $\eta = \eta_0 + \eta_1$ gives $\boldsymbol{\tau} = (\boldsymbol{\tau}_0 + \boldsymbol{\tau}_{ac}) + \boldsymbol{\tau}_1$, where the steady part $\boldsymbol{\tau}_0 + \boldsymbol{\tau}_{ac}$ contains terms $\eta_0\boldsymbol{\nabla}\boldsymbol{v}_0$ and $\langle\eta_1\boldsymbol{\nabla}\boldsymbol{v}_1\rangle$, respectively, and the acoustic part $\boldsymbol{\tau}_1$ contains terms $\eta_0\boldsymbol{\nabla}\boldsymbol{v}_1$. The governing equations for the acoustic temperature T_1^{fl}, pressure p_1, and velocity $\boldsymbol{v}_1$ in the fluid as well as temperature T_1^{sl} and displacement $\boldsymbol{u}_1$ in the solid, become

$$-i\omega T_1^{fl} + i\omega(\gamma-1)\frac{\kappa_{s0}}{\alpha_{p0}} p_1 = D_0^{th}\nabla^2 T_1^{fl}, \tag{2a}$$

$$-i\omega\alpha_{p0} T_1^{fl} + i\omega\kappa_{T0} p_1 = \boldsymbol{\nabla}\cdot\boldsymbol{v}_1, \tag{2b}$$

$$-i\omega\rho_0\boldsymbol{v}_1 = -\boldsymbol{\nabla}p_1 + \boldsymbol{\nabla}\cdot\boldsymbol{\tau}_1, \tag{2c}$$

$$-i\omega T_1^{sl} - i\omega\frac{\gamma-1}{\alpha_{p0}}\boldsymbol{\nabla}\cdot\boldsymbol{u}_1 = D_0^{th}\nabla^2 T_1^{sl}, \tag{2d}$$

$$-\omega^2\rho_0\boldsymbol{u}_1 = -\frac{\alpha_{p0}}{\kappa_{T0}}\boldsymbol{\nabla}T_1^{sl} + (c_{lo}^2 - c_{tr}^2)\boldsymbol{\nabla}(\boldsymbol{\nabla}\cdot\boldsymbol{u}_1) + c_{tr}^2\nabla^2\boldsymbol{u}_1. \tag{2e}$$

Similarly, the governing equations for the steady temperature T_0^{fl}, pressure p_0, and streaming velocity $\boldsymbol{v}_0$ in the fluid, as well as the temperature T_0^{sl} in the solid, are

$$0 = -\nabla \cdot (\rho_0 v_0) + \dot{\rho}_{ac} \tag{3a}$$

$$0 = -\nabla p_0 + \nabla \cdot \tau_0 - \nabla \cdot (\rho_0 v_0 v_0) + \hat{f}_{ac} \tag{3b}$$

$$0 = \nabla \cdot [k_0^{th} \nabla T_0^{fl}] - c_p \rho_0 v_0 \cdot \nabla T_0^{fl} + P_{ac}^{fl} + P, \tag{3c}$$

$$0 = \nabla \cdot (k_0^{th} \nabla T_0^{sl}) + P_{ac}^{sl} + P, \tag{3d}$$

with the acoustic-product source terms given by

$$\dot{\rho}_{ac} = -\nabla \cdot \langle \rho_1 v_1 \rangle, \tag{3e}$$

$$\hat{f}_{ac} = \nabla \cdot [-\rho_0 \langle v_1 v_1 \rangle + \tau_{ac}], \tag{3f}$$

$$P_{ac}^{sl} = \nabla \cdot \langle k_1^{th} \nabla T_1^{sl} \rangle, \tag{3g}$$

$$P_{ac}^{fl} = \nabla \cdot [\langle k_1^{th} \nabla T_1^{fl} \rangle - \langle p_1 v_1 \rangle + \langle v_1 \cdot \tau_1 \rangle$$
$$- \rho_0 c_{p0} \langle T_1^{fl} v_1 \rangle] - c_p \langle \rho_1 v_1 \rangle \cdot \nabla T_0^{fl}. \tag{3h}$$

Here, P_{ac} and P are the power density supplied internally by the acoustic fields and externally by given sources, respectively, and we have neglected small terms $|\rho_1 v_0| \ll |\rho_0 v_1|$ and $|\eta_1 v_0| \ll |\eta_0 v_1|$, which holds for typical acoustofluidic devices. Moreover, since the thermal expansion of the solid due to the gradients in T_0 is minute, we have assumed $u_0 = 0$. The boundary conditions are continuous velocity and stress fields across the oscillating fluid-solid interface for both steady (including the Stokes drift) and acoustic fields, as detailed in Ref. [10]. A no-stress condition is applied on the exterior surface, except at the actuation region, where a displacement condition $u_1 = u_{exc}$ is applied to u_1.

We note that in the bulk, the acoustic body force takes the form $\hat{f}_{ac} = f_{ac} + \nabla \langle \mathcal{L}_{ac} \rangle$. The gradient term is absorbed in the pressure gradient $-\nabla p_0$, leaving the part f_{ac} of the acoustic body force, which drives thermoacoustic streaming [7,8] in the bulk of the fluid [10],

$$f_{ac} = -\frac{1}{4}|v_1|^2 \nabla \rho_0 + \left[1 - \frac{2a_\eta(\gamma - 1)}{\beta + 1}\right] \frac{\Gamma \omega}{c_0^2} \langle v_1 p_1 \rangle$$
$$- \frac{1}{4}|p_1|^2 \nabla \kappa_s + 2a_\eta \eta_0 (\gamma - 1) \frac{\omega}{c_0^2} \langle i v_1 \cdot \nabla v_1 \rangle \tag{4a}$$

$$\approx -\frac{1}{4}\left[|p_1|^2 \left(\frac{\partial \kappa_s}{\partial T}\right)_{T_0} + |v_1|^2 \left(\frac{\partial \rho}{\partial T}\right)_{T_0}\right] \nabla T_0. \tag{4b}$$

Here, the last expression is valid for sufficiently large temperature gradients ∇T_0 in the bulk. In the usual perturbative limit, the first-order fields p_1, v_1, and u_1 depend linearly on the actuation amplitude u_{exc}. As time-averaged products of these fields are sources for the time-averaged second-order fields T_2 and v_2, the spatial patterns of the latter are independent of u_{exc}, whereas their amplitudes scale as $u_{exc}^2 \propto E_{ac} = \frac{1}{4}\kappa_s|p_1|^2 + \frac{1}{2}\rho_0|v_1|^2$. Notably, since $|p_1|^2$,

$|v_1|^2$, and ∇T_0 all scale as $u_{exc}^2 \propto E_{ac}$, and f_{ac} in Eq. (4b)) scales as E_{ac}^2, f_{ac} leads to nonperturbative effects in the thermoviscous streaming v_0, such as an E_{ac}-dependent spatial pattern and an amplitude nonlinear in E_{ac}. These effects will dominate over the usual perturbative response at sufficiently high values of E_{ac}, as shown experimentally and numerically below.

Experimental method.—The experiments were performed on the glass-silicon chip of Fig. 1(d) glued to a piezoelectric transducer, the same as in Ref. [28]. The system was driven at the resonance frequency 1.97 MHz using input powers $P_{in} = 6.1, 86.8$, and 182.5 mW, resulting in the energy density $E_{ac} = 27.2 \pm 1.1, 388.7 \pm 15.9$, and 817.3 ± 33.5 J/m³. When less than 140 J/m³, E_{ac} is determined from the focusing of 4.9-μm-diameter polystyrene particles at 140 fps using confocal microparticle image velocimetry (μPIV) [9]. When greater than 140 J/m³, E_{ac} is estimated using the proportionality $E_{ac} \propto P_{in}$. To measure E_{ac} accurately, the confocal μPIV technique only captures the particle motion near the focal plane (channel midheight), excluding particles near the top and bottom walls influenced by hydrodynamic and acoustic particle-wall interactions [11]. The acoustic streaming for each E_{ac} was measured at 10 to 60 fps by tracking 0.5-μm-diameter particles using a defocusing-based 3D particle tracking technique [32–34]. To avoid the resonance frequency shift due to the temperature rise of the transducer under moderate (86.8 mW) and high (182.5 mW) P_{in}, each measurement was run for only 2 s and repeated 100 times to improve the statistics, resulting in 7800–12 000 recorded frames for each driving condition. For further experimental details see Sec. S2 in the Supplemental Material [29].

Numerical method.—The numerical simulation of the model is carried out using the commercial finite-element software COMSOL Multiphysics [35] as described in Ref. [7] for the perturbative case, but extended with the iterative procedure described above to handle the nonperturbative case; see details in Ref. [10]. The only free parameter is the displacement amplitude u_{exc}, which is fixed to obtain the measured value of E_{ac}. A sample script is provided in Sec. S3 in the Supplemental Material [29].

Results and discussion.—The simulation and experimental results in Fig. 2 show how the streaming v_0 and temperature T_0 in a standard acoustofluidic device undergo a clear qualitative transition as E_{ac} increases. In the perturbative regime at low $E_{ac} \lesssim 30$ J/m³ shown in Fig. 2(a), v_0 is dominated by the boundary-driven streaming sketched in Fig. 1(b) that scales linearly with E_{ac} and exhibits the usual four flow rolls. Because of friction in the viscous boundary layers, heat is generated both at the top and bottom of the channel. At the bottom, this heat is removed efficiently because of the high heat conductivity of silicon. At the top, however, the heat is removed less efficiently by the lower heat conductivity of glass, and a steady temperature gradient ∇T_0 is established, which
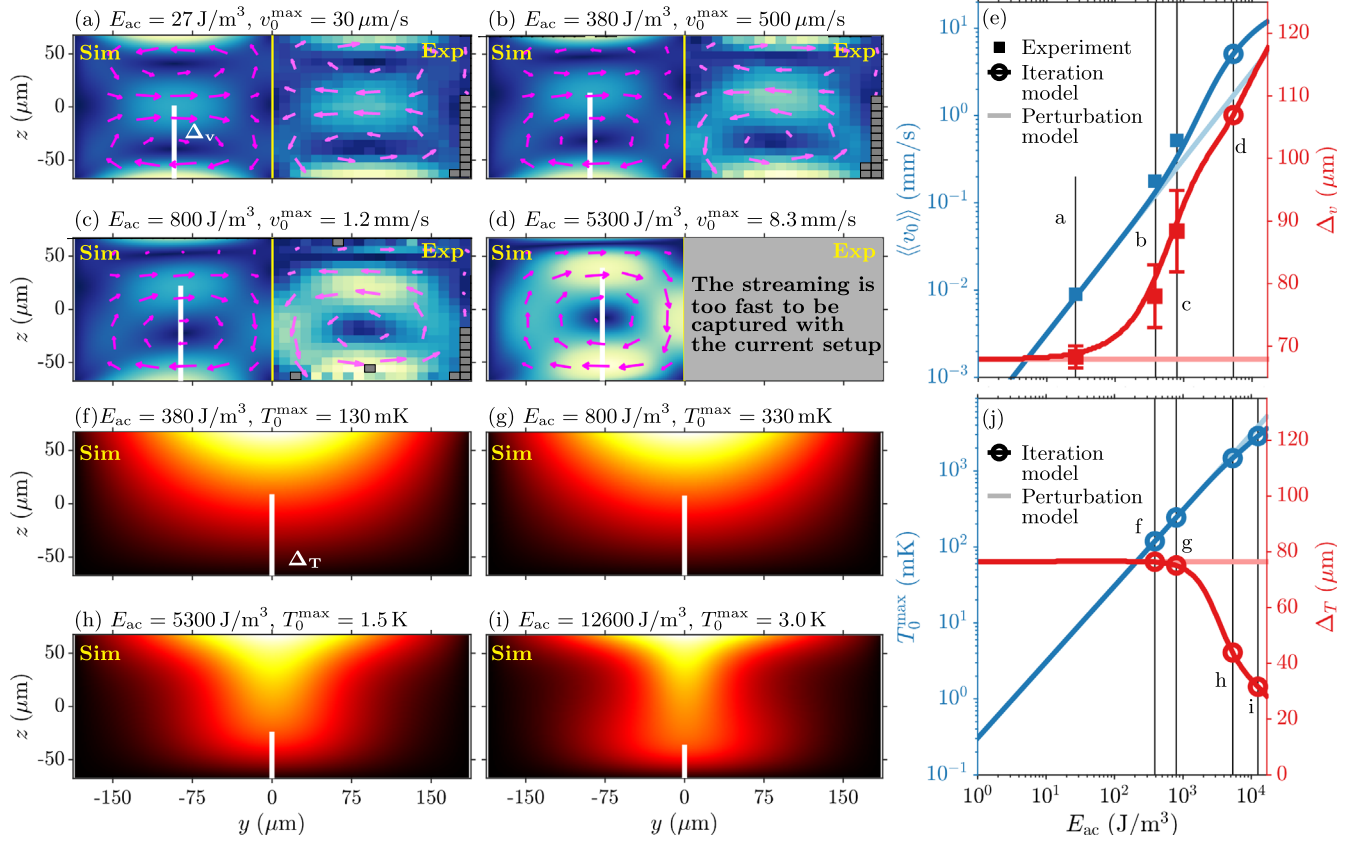
FIG. 2. Simulation and experiment on $\boldsymbol{v}_0$ and T_0 (with z-axis mirror symmetry) in the microchannel. (a)–(d) Vector plot of $\boldsymbol{v}_0$ and color plot of $|\boldsymbol{v}_0|$ from 0 (blue) to v_0^{max} (yellow). For each E_{ac}, the left half is simulation and the right half is experiment. Δ_v (white bar) is the height where v_{0y} is maximal. (e) Plots of simulated (full curves and ○) and measured (■) $\langle\!\langle v_0 \rangle\!\rangle$ and Δ_v vs E_{ac}, showing the transition from boundary-driven to bulk-driven streaming. The error bars on experimental $\langle\!\langle v_0 \rangle\!\rangle$ and E_{ac} are within the square markers [29]. The round markers (○) represent the simulations shown in panels (d) and (f)–(i). (f)–(i) Color plot of simulated temperature increase T_0 from 0 (black) to T_0^{max} at four E_{ac}. Δ_T (white bar) is the height where $T_0 = \frac{1}{2}T_0^{\mathrm{max}}$. (j) Plots of simulated T_0^{max} and Δ_T vs E_{ac} showing a transition from diffusion-dominated to convection-dominated heat transport.

together with Eq. (4b) explains the temperature T_0 seen in Fig. 2(f): The acoustic body force $\boldsymbol{f}_{\mathrm{ac}}$ points toward the high temperature at the top, and it is strongest at the pressure antinodes at the sides [7,8]. Consequently, $\boldsymbol{f}_{\mathrm{ac}}$ pushes liquid from the sides up toward the top center, which induces a backflow down along vertical center axis. The resulting streaming pattern consists of two flow rolls, one in each side of the channel. This bulk-driven nonperturbative pattern is seen in Fig. 2(d) at the high $E_{\mathrm{ac}} = 5300$ J/m^3, where $\boldsymbol{v}_0$ is completely dominated by the thermoacoustic streaming. The transition from boundary-driven streaming at low E_{ac} to bulk-driven streaming at high E_{ac} is studied qualitatively in Figs. 2(a)–2(d) and quantitatively in Fig. 2(e). During the transition in Figs. 2(b)–2(c), the two bottom streaming rolls expand, and the two top rolls shrink, at $E_{\mathrm{ac}} = 380$ and 800 J/m^3, respectively. The bottom rolls expand, because they rotate the same way as the two thermoacoustic streaming rolls.

This transition is studied quantitatively in Fig. 2(e) by plotting measured (3 points) and simulated (156 points)

values of the spatial average $\langle\!\langle v_0 \rangle\!\rangle$ of the magnitude $v_0 = |\boldsymbol{v}_0|$ of the streaming velocity and the vertical distance Δ_v (thick white line) from the bottom of the channel to the position where the maximum horizontal streaming velocity $\max(v_{0y})$ toward the center occurs. In the log-log plot (dark blue), the perturbative result $\langle\!\langle v_0 \rangle\!\rangle \propto E_{\mathrm{ac}}$ is valid up to $E_{\mathrm{ac}} \approx 400$ J/m^3, but at higher values $\langle\!\langle v_0 \rangle\!\rangle$ increases faster. A stronger signal is seen in the log-lin plot (dark red), where the perturbative result $\Delta_v \simeq$ const only holds for $E_{\mathrm{ac}} \lesssim 30$ J/m^3, after which point Δ_v increases with increasing E_{ac}.

As $\boldsymbol{v}_0$ increases, the heat convection $-c_p\rho_0\boldsymbol{v}_0 \cdot \boldsymbol{\nabla}T_0^{\mathrm{fl}}$ in Eq. (3c) affects the temperature field ever more strongly, as seen in Figs. 2(f)–2(i) for $E_{\mathrm{ac}} = 380$, 800, 5300, and 12 600 J/m^3, and it becomes important when the Péclet number $|\boldsymbol{v}_0|H/D^{\mathrm{th}}$ exceeds unity for $|\boldsymbol{v}_0| \gtrsim 1$ mm/s, consistent with Figs. 2(f)–2(j). Qualitatively, we see that for $E_{\mathrm{ac}} \gtrsim 800$ J/m^3, the two flow rolls pull the temperature profile down along the vertical center axis. We quantify this effect by the maximum temperature T_0^{max} and the vertical

distance Δ_T along the center axis from the bottom edge to the point where $T_0 = \frac{1}{2}T_0^{\max}$. The thermoacoustic streaming increases the heat transport from the fluid-glass interface to the silicon wafer; thus $T_0^{\max}$ increases less steeply than the perturbative result, $T_0^{\max} \propto E_{ac}$, as seen in the log-log plot (blue) of $T_0^{\max}$ vs E_{ac} for $E_{ac} \gtrsim 5000 \text{ J/m}^3$ in Fig. 2(j). A stronger signal is seen in the log-lin plot (dark red), where the perturbative result $\Delta_T \simeq \text{const}$ only holds for $E_{ac} \lesssim 400 \text{ J/m}^3$, after which point Δ_T decreases with increasing E_{ac}.

Conclusion.—In this Letter we have shown numerically and experimentally that the acoustic streaming in a standard microscale acoustofluidic device is changed qualitatively for moderately high acoustic energy densities $E_{ac} \gtrsim 400 \text{ J/m}^3$. We have explained this effect by a nonperturbative model, in which a transition from boundary-driven to bulk-driven acoustic streaming occurs, as the acoustic body force $\boldsymbol{f}_{ac}$ begins to dominate the streaming at increased E_{ac} due to the internal heating generated in the viscous boundary layers. We have shown good qualitative and quantitative agreement between our model predictions and experimental data. The iterative model can easily be extended to materials other than silicon, glass, and water, such as we have done in the perturbative model with iodixanol solutions [36], rubber (polydimethylsiloxane) [37,38], aluminum [38], and polymer (PMMA) [39], and with oil in the iterative model itself [10].

$E_{ac} \gtrsim 400 \text{ J/m}^3$ can easily be obtained in standard acoustofluidic devices, for which $E_{ac} \approx 10\text{–}50 \text{ J/m}^3 \times [U_{pp}/(1 \text{ V})]^2$ has been reported, U_{pp} being the voltage applied to the transducer [12,40–42], and higher E_{ac} could be obtained by optimized actuation schemes [9,39,43,44]. The physical understanding of how such acoustofluidic devices behave at high E_{ac} is important for the continued development of high-throughput devices of particular relevance in biotech and clinical applications.

---

[*] jonashj@fysik.dtu.dk
[†] wei.qiu@bme.lth.se
[‡] bruus@fysik.dtu.dk

[1] J. T. Karlsen and H. Bruus, Forces acting on a small particle in an acoustical field in a thermoviscous fluid, Phys. Rev. E **92**, 043010 (2015).

[2] T. Baasch, A. Pavlic, and J. Dual, Acoustic radiation force acting on a heavy particle in a standing wave can be dominated by the acoustic microstreaming, Phys. Rev. E **100**, 061102(R) (2019).

[3] Lord Rayleigh, On the circulation of air observed in Kundt's tubes, and on some allied acoustical problems, Phil. Trans. R. Soc. London **175**, 1 (1884).

[4] C. Eckart, Vortices and streams caused by sound waves, Phys. Rev. **73**, 68 (1948).

[5] G. Chini, Z. Malecha, and T. Dreeben, Large-amplitude acoustic streaming, J. Fluid Mech. **744**, 329 (2014).

[6] G. Michel and C. Gissinger, Cooling by Baroclinic Acoustic Streaming, Phys. Rev. Appl. **16**, L051003 (2021).

[7] J. H. Joergensen and H. Bruus, Theory of pressure acoustics with thermoviscous boundary layers and streaming in elastic cavities, J. Acoust. Soc. Am. **149**, 3599 (2021).

[8] W. Qiu, J. H. Joergensen, E. Corato, H. Bruus, and P. Augustsson, Fast Microscale Acoustic Streaming Driven by a Temperature-Gradient-Induced Non-Dissipative Acoustic Body Force, Phys. Rev. Lett. **127**, 064501 1 (2021).

[9] W. Qiu, T. Baasch, and T. Laurell, Enhancement of Acoustic Energy Density in Bulk-Wave-Acoustophoresis Devices using Side Actuation, Phys. Rev. Appl. **17**, 044043 (2022).

[10] J. H. Joergensen and H. Bruus, companion paper, Theory and modeling of nonperturbative effects in thermoviscous acoustofluidics, Phys. Rev. E **107**, 015106 (2023).

[11] R. Barnkob, P. Augustsson, T. Laurell, and H. Bruus, Acoustic radiation- and streaming-induced microparticle velocities determined by microparticle image velocimetry in an ultrasound symmetry plane, Phys. Rev. E **86**, 056307 (2012).

[12] P. B. Muller, M. Rossi, A. G. Marin, R. Barnkob, P. Augustsson, T. Laurell, C. J. Kähler, and H. Bruus, Ultrasound-induced acoustophoretic motion of microparticles in three dimensions, Phys. Rev. E **88**, 023006 (2013).

[13] P. B. Muller and H. Bruus, Numerical study of thermoviscous effects in ultrasound-induced acoustic streaming in microchannels, Phys. Rev. E **90**, 043016 (2014).

[14] J. S. Bach and H. Bruus, Theory of pressure acoustics with viscous boundary layers and streaming in curved elastic cavities, J. Acoust. Soc. Am. **144**, 766 (2018).

[15] M. A. Solovchuk, T. W. Sheu, M. Thiriet, and W.-L. Lin, On a computational study for investigating acoustic streaming and heating during focused ultrasound ablation of liver tumor, Appl. Therm. Eng. **56**, 62 (2013).

[16] M. A. Solovchuk, M. Thiriet, and T. W. Sheu, Computational study of acoustic streaming and heating during acoustic hemostasis, Appl. Therm. Eng. **124**, 1112 (2017).

[17] A. Sedaghatkish, M. Rezaeian, H. Heydari, A. M. Ranjbar, and M. Soltani, Acoustic streaming and thermosensitive liposomes for drug delivery into hepatocellular carcinoma tumor adjacent to major hepatic veins; an acoustics–thermal–fluid-mass transport coupling model, Int. J. Therm. Sci. **158**, 106540 (2020).

[18] A. Ozcelik, D. Ahmed, Y. Xie, N. Nama, Z. Qu, A. A. Nawaz, and T. J. Huang, An acoustofluidic micromixer via bubble inception and cavitation from microchannel sidewalls, Anal. Chem. **86**, 5083 (2014).

[19] M. V. Patel, I. A. Nanayakkara, M. G. Simon, and A. P. Lee, Cavity-induced microstreaming for simultaneous on-chip pumping and size-based separation of cells and particles, Lab Chip **14**, 3860 (2014).

[20] H. Bachman, C. Chen, J. Rufo, S. Zhao, S. Yang, Z. Tian, N. Nama, P.-H. Huang, and T. J. Huang, An acoustofluidic device for efficient mixing over a wide range of flow rates, Lab Chip **20**, 1238 (2020).

[21] C. Zhang, P. Brunet, L. Royon, and X. Guo, Mixing intensification using sound-driven micromixer with sharp edges, Chem. Eng. J. **410**, 128252 (2021).

[22] M. Wiklund, R. Green, and M. Ohlin, Acoustofluidics 14: Applications of acoustic streaming in microfluidic devices, Lab Chip **12**, 2438 (2012).

[23] D. J. Collins, Z. Ma, and Y. Ai, Highly localized acoustic streaming and size-selective submicrometer particle concentration using high frequency microscale focused acoustic fields, Anal. Chem. **88**, 5513 (2016).

[24] D. J. Collins, Z. Ma, J. Han, and Y. Ai, Continuous micro-vortex-based nanoparticle manipulation via focused surface acoustic waves, Lab Chip **17**, 91 (2017).

[25] J. D. Adams, C. L. Ebbesen, R. Barnkob, A. H. J. Yang, H. T. Soh, and H. Bruus, High-throughput, temperature-controlled microchannel acoustophoresis device made with rapid prototyping, J. Micromech. Microeng. **22**, 075017 (2012).

[26] M. Antfolk, C. Magnusson, P. Augustsson, H. Lilja, and T. Laurell, Acoustofluidic, label-free separation and simultaneous concentration of rare tumor cells from white blood cells, Anal. Chem. **87**, 9322 (2015).

[27] A. Urbansky, F. Olm, S. Scheding, T. Laurell, and A. Lenshof, Label-free separation of leukocyte subpopulations using high throughput multiplex acoustophoresis, Lab Chip **19**, 1406 (2019).

[28] W. Qiu, H. Bruus, and P. Augustsson, Particle-size-dependent acoustophoretic motion and depletion of micro-and nano-particles at long timescales, Phys. Rev. E **102**, 013108 (2020).

[29] See Supplemental Material at http://link.aps.org/supplemental/10.1103/PhysRevLett.130.044001 for details about material parameters, experimental methods, and a COMSOL Multiphysics sample script, which includes Refs. [30,31].

[30] W. Thielicke and E. Stamhuis, PIVlab–towards user-friendly, affordable and accurate digital particle image velocimetry in MATLAB, J. Open Res. Software **2**, e30 (2014).

[31] W. Qiu, J. T. Karlsen, H. Bruus, and P. Augustsson, Experimental Characterization of Acoustic Streaming in Gradients of Density and Compressibility, Phys. Rev. Appl. **11**, 024018 (2019).

[32] R. Barnkob, C. J. Kähler, and M. Rossi, General defocusing particle tracking, Lab Chip **15**, 3556 (2015).

[33] R. Barnkob and M. Rossi, General defocusing particle tracking: Fundamentals and uncertainty assessment, Exp. Fluids **61**, 110 (2020).

[34] M. Rossi and R. Barnkob, A fast and robust algorithm for general defocusing particle tracking, Meas. Sci. Technol. **32**, 014001 (2020).

[35] COMSOL Multiphysics 5.6 (2020), http://www.comsol.com.

[36] J. T. Karlsen, W. Qiu, P. Augustsson, and H. Bruus, Acoustic Streaming and its Suppression in Inhomogeneous Fluids, Phys. Rev. Lett. **120**, 054501 (2018).

[37] N. R. Skov, P. Sehgal, B. J. Kirby, and H. Bruus, Three-Dimensional Numerical Modeling of Surface-Acoustic-Wave Devices: Acoustophoresis of Micro- and Nanoparticles Including Streaming, Phys. Rev. Appl. **12**, 044028 (2019).

[38] W. N. Bodé, L. Jiang, T. Laurell, and H. Bruus, Micro-particle acoustophoresis in aluminum-based acoustofluidic devices with PDMS covers, Micromachines **11**, 292 (2020).

[39] F. Lickert, M. Ohlin, H. Bruus, and P. Ohlsson, Acoustophoresis in polymer-based microfluidic devices: Modeling and experimental validation, J. Acoust. Soc. Am. **149**, 4281 (2021).

[40] R. Barnkob, P. Augustsson, T. Laurell, and H. Bruus, Measuring the local pressure amplitude in microchannel acoustophoresis, Lab Chip **10**, 563 (2010).

[41] P. Augustsson, R. Barnkob, S. T. Wereley, H. Bruus, and T. Laurell, Automated and temperature-controlled micro-PIV measurements enabling long-term-stable microchannel acoustophoresis characterization, Lab Chip **11**, 4152 (2011).

[42] R. Barnkob, I. Iranmanesh, M. Wiklund, and H. Bruus, Measuring acoustic energy density in microchannel acoustophoresis using a simple and rapid light-intensity method, Lab Chip **12**, 2337 (2012).

[43] M. Bora and M. Shusteff, Efficient coupling of acoustic modes in microfluidic channel devices, Lab Chip **15**, 3192 (2015).

[44] A. Tahmasebipour, L. Friedrich, M. Begley, H. Bruus, and C. Meinhart, Toward optimal acoustophoretic microparticle manipulation by exploiting asymmetry, J. Acoust. Soc. Am. **148**, 359 (2020).

[45] DefocusTracker (2021), https://defocustracking.com/.